Research Article

Morphosynthesis of Zn-Substituted Stoichiometric and Carbonate Hydroxyapatite Nanoparticles and Their Cytotoxicity in Fibroblasts

Tania Guadalupe Peñaflor Galindo,[1] Takuya Kataoka,[1] and Motohiro Tagaya[1,2]

[1]Department of Materials Science and Technology, Nagaoka University of Technology, 1603-1 Kamitomioka,
 Nagaoka, Niigata 940-2188, Japan
[2]Top Runner Incubation Center for Academia-Industry Fusion, Nagaoka University of Technology,
 1603-1 Kamitomioka, Nagaoka, Niigata 940-2188, Japan

Correspondence should be addressed to Motohiro Tagaya; tagaya@mst.nagaokaut.ac.jp

Hydroxyapatite ($Ca_{10}(PO_4)_3(OH)_2$) (HAp) is crystallographically and chemically similar to the human hard tissues and has been widely researched. The naturally formed HAp has some impurities of some ions, which provides the biocompatibility as well as the nanosized morphologies in the tissues. In this study, the morphosynthesis of zinc-substituted stoichiometric and carbonate hydroxyapatite (Zn:HAp and Zn:CAp) nanoparticles was investigated from the reagents of $CaCl_2$, $ZnCl_2$, and K_2HPO_4. The initial $(Ca + Zn)/P$ ratios of 1.67 and 2.00 were adjusted by the initial $ZnCl_2$ amount at the $Zn/(Ca + Zn)$ concentration of 0.0–10 mol%. The crystalline sizes of the nanoparticles decreased with increasing the Zn ion amount, suggesting that the Zn substitution significantly suppressed the crystal growth. TEM images of the nanoparticles indicated that all the crystalline sizes are less than 100 nm and the needle-like shapes were significantly changed to spherical shapes with increasing the Zn ion substitution to resultantly exhibit the higher surface areas as well as the nanoparticle aggregation states. Furthermore, all the nanoparticle films electrically plated on a silicone substrate give no cytotoxicity, and the Zn:CAp nanoparticle films significantly provided the bioactive properties for fibroblast ingrowth, suggesting the effect of Zn and carbonate ions on the cytocompatibility.

1. Introduction

The composition of human bone is an inorganic/organic nanohybrid consisting of calcium phosphates as hydroxyapatite (HAp, $Ca_{10}(PO_4)_6(OH)_2$) phase and organic compounds such as collagen. In the inorganic phases, the HAp often contains the small amount of various ions such as carbonate, sodium, magnesium, and zinc (Zn) ions to generate the biocompatibility as well as the nanofunctions in the animal body. Thus, the submicroscopic purity and morphology control of calcium phosphates such as HAp (e.g., bone-like apatite nanoparticles [1]) at the nanoscales devising synthetic method are very important for the biomedical applications.

The HAp-based bioceramics are widely used as highly biocompatible implants due to their chemical similarity to the biological hard tissues, providing the various biofunctions such as stability and hardness [2]. HAp has also been investigated for the application use as the bone filling materials [3–6] and as drug delivery carriers [7–11], and the protein adsorption and cell adhesion on the HAp have been reported so far [12, 13]. However, the detailed features depending on the morphology and surface properties based on the nanoscale control technique have not been clarified in detail. Thus, the understanding of the morphosynthesis of the HAp nanoparticles containing various ions is of great importance for making the nature of biocompatibility clear.

For improving the biocompatibility by the heterogeneous ions, the substitution of carbonate ions into the HAp structure is very important. Generally, CO_2 can be dissolved into a synthetic solution as carbonate ions and eventually incorporated into the structure, replacing PO_4^{3-} or OH^- ions in the structure [14]. In the synthesis in the presence of

sodium or potassium ions, these ions are partially substituted with the Ca^{2+} ions of the structure and are important for promoting new tissue (e.g., bone formation). For improving low antibacterial activity of HAp for the long term biomedical usage, the substitution of Ag^+, Zn^{2+}, Ti^{4+}, and Cu^{2+} into the HAp structures provides not only bone-like crystallinity but also antibacterial properties [15, 16]. In particular, Zn ion is present in all biological hard tissues and is thought to stimulate bone mineralization and help in pathological calcification. Furthermore, the Zn ion also plays a vital role in the maintenance of membrane structure, function, protein synthesis, DNA synthesis, mitosis, and cell proliferation [17–19]. However, the detailed features of the morphology and surface properties of Zn-substituted HAp under the other ion at the nanoscales have not been clarified. Thus, the investigation of the morphosynthesis of Zn-substituted HAp nanoparticles is of great importance.

In this study, Zn(II) ion (Zn^{2+})-substituted stoichiometric and carbonate HAp nanoparticles, which are abbreviated as Zn:HAp and Zn:CAp, were synthesized at the initial molar ratio of (Ca + Zn)/P ratios at 1.67 and 2.00 The morphosynthesis was conducted by a wet chemical method and the calcium and phosphate precursors were mixed and then precipitated under basic condition. Although many chemical synthetic routes for the HAp nanoparticles have been developed using hydrothermal, coprecipitation, sol-gel, and combustion techniques [20], the wet chemical method for the highly controllable morphology and chemical component was focused in this study. The crystal growth at the higher Zn concentration was investigated and compared between stoichiometric and carbonate HAp nanoparticles. Furthermore, the cytotoxicity in NIH3T3 fibroblasts of the nanoparticle films electrically plated on a silicone substrate was investigated.

2. Experimental

2.1. Materials.
Potassium phosphate dibasic trihydrate ($K_2HPO_4 \cdot 3H_2O$), zinc chloride ($ZnCl_2$), and sodium hydroxide (NaOH) as the special grade chemicals were purchased from Wako Chemical Co., Ltd. Calcium chloride ($CaCl_2$) as the special grade chemical was purchased from Nacalai Tesque, Inc. All the reagents were used without further purification.

2.2. Synthesis of Zn-Substituted Hydroxyapatite Nanoparticles.
0.024 mol of $K_2HPO_4 \cdot 3H_2O$ was completely dissolved into 100 mL of deionized water at 40°C and then stirred for 60 min to prepare phosphate solution. The aqueous solution containing 0.04 mol of both $CaCl_2$ and $ZnCl_2$ was added into the phosphate solution at the drop rate of 5 mL/min at 40°C and then stirred for 60 min. The pH value of the mixture solution was adjusted up to 12 using 1 N-NaOH aqueous solution. After the aging period for 60 min, the precursor solution was then refluxed at 40°C for 24 h. The solution was centrifuged (10000 g, for 15 min, at 4°C) and the sediment solid was washed with ultrapure water 3 times. The washed

product was dried at 100°C for 24 h under air. Here, the Zn-substituted HAp nanoparticles were synthesized from the initial molar ratio of (Ca + Zn)/P at 1.67 or 2.00 with the different initial Zn concentrations to the total (Ca + Zn) at 0.0, 2.5, 5.0, and 10 mol%, and these resultant samples form the ratio of (Ca + Zn)/P at 1.67 and 2.00 was abbreviated as X—Zn:HAp or X—Zn:CAp, respectively. The X is the Zn/(Ca + Zn) value, which is 0.0, 2.5, 5.0, and 10.

2.3. Characterization.
The contents (mol%) of the atomic elements (Ca, Zn, P, and C) were determined using a wavelength dispersive X-ray fluorescence spectrometry (XRF) (ZSX Primus II, Rigaku Co., Ltd.).

Fourier Transform Infrared (FTIR) spectra were recorded on a Jasco FT/IR-4100 spectrometer. The spectra were obtained at the wavenumbers between 400 and 4000 cm^{-1} with an accumulation of 128 times and resolution of 2.0 cm^{-1}.

XRD patterns were recorded by a Smart Lab diffractometer (Rigaku Co., Ltd.) using monochromatized CuKα radiation. The crystalline phases were determined by comparing the X-ray patterns with HAp (JCPDS 9-432) standard, and the lattice parameters were determined by Rietveld refinement of the diffraction profiles with a PDXL2 program. For the hexagonal cell parameters a and c of the crystallographic system, the relationship between the distance (d) of two adjacent net planes and the plane (hkl) Miller indices of the reflection planes [20, 21] is given by

$$d = \frac{1}{\sqrt{(4/3)\left(\left(h^2 + hk + k^2\right)/a^2\right) + l^2/c^2}}. \tag{1}$$

The crystalline sizes of the nanoparticles were estimated using Scherrer equation of

$$D_{hkl} = \frac{K\lambda}{\beta \cos\theta}, \tag{2}$$

where D_{hkl} indicates the crystalline size, λ is the X-ray wavelength (0.15418 nm), β is the full width at half maximum (in radians) of 002 and 300 diffraction peak, and θ is the diffraction angle and K is 0.9 [20, 22].

The nitrogen (N_2) adsorption/desorption isotherms were measured at −196°C on TriStar II (Shimadzu Co., Ltd.). Prior to the measurements, the samples were dried at 100°C under vacuum for 3 h. The specific surface area (S_{BET}) values were calculated by means of the Brunauer-Emmett-Teller (BET) method [23] using a linear plot over the range of P/P_0 0.05–0.30. Pore size distributions were derived from adsorption isotherms by the Barrett-Joyner-Halenda (BJH) method [24].

The morphology was observed by transmission electron microscopy (TEM) with a JEM-1400 (JEOL Co., Ltd.). The ethanoic suspension at the solid concentration of 0.01 wt% was dropped onto a carbon-coated copper (Cu) grid (Cu 200-A mesh, Okenshoji Co., Ltd.), and the grid was dried in desiccator under nitrogen atmosphere for 1 day. The nanoparticles were examined in bright mode at the magnifications typically up to ×1,000,000 under an accelerating voltage of 120 kV.

TABLE 1: Resultant chemical compositions of the Zn:HAp and Zn:CAp nanoparticles with the different Zn concentrations.

Sample	Ca (mol%)	Zn (mol%)	P (mol%)	C (mol%)	(Ca + Zn)/P ratio	Zn conc. (mol%)
0.0—Zn:HAp	0.87	0.00	0.53	0.22	1.64	0.00
2.5—Zn:HAp	0.86	0.01	0.53	0.26	1.64	1.15
5.0—Zn:HAp	0.82	0.02	0.52	0.27	1.62	2.38
10—Zn:HAp	0.73	0.04	0.51	0.39	1.51	5.19
0.0—Zn:CAp	0.93	0.00	0.48	0.24	1.94	0.00
2.5—Zn:CAp	0.88	0.01	0.47	0.35	1.89	1.12
5.0—Zn:CAp	0.87	0.02	0.47	0.37	1.89	2.25
10—Zn:CAp	0.82	0.04	0.47	0.42	1.83	4.65

2.4. Cytotoxicity Evaluation. The synthesized nanoparticles were ultrasonically dispersed in ethanol at the solid concentration of 1 wt%. The silicone substrate surface was precoated with a thin titanium layer at the thickness of ca. 5 nm by a DC sputtering. Then, the Ti-coated silicone was used as the working electrodes (counter electrode: Al substrate) and the DC voltage of 100 V/cm was applied for 1 min in the suspension to electrophoretically deposit the nanoparticles on the silicone surfaces. The surplus nanoparticles were removed by an ultrasonic treatment (28 kHz, 100 W) for 1 min in ethanol to obtain the highly transparent Zn:HAp and Zn:CAp nanoparticle thin films. The detailed electrophoretic fabrication of Zn:HAp and Zn:CAp nanoparticle films on silicone will be reported in the other journal soon by our laboratory.

The cytocompatibility was examined using the Zn:HAp and Zn:CAp nanoparticle films. The films were kept in phosphate buffered saline (PBS) and sterilized with ethanol/water solutions (50 and 70 vol%) and then rinsed twice with PBS and fetal bovine serum (FBS)/DMEM solution. The NIH3T3 fibroblast suspension was seeded at the density of 8000 cells/cm^2 on the film surfaces and cultured at 37°C under 5%-CO$_2$ for 48 h and rinsed with 1 mL of FBS/DMEM and PBS. The washed surfaces of adhered cells were immediately fixed with formaldehyde and then were observed by an optical microscopy (Olympus Co., Ltd., CKX41) to obtain the adhered cell density and area. Here, bare silicone substrate without coating was used as the reference.

3. Results and Discussion

3.1. Chemical Compositions and Bonds. Table 1 shows the mole percentage of each element found in the synthesized nanoparticles by the XRF analysis. The Ca content decreased with increasing the Zn ion amount and the maximum substituted Zn content is ca. 5 mol% from the initial concentration of 10 mol%, indicating the successful Zn ion incorporation into the HAp structures. Furthermore, the C content increased with increasing the Zn ion amount and that in the Zn:CAp was higher than that in the Zn:HAp, indicating the carbonate ion (e.g., $CO_3{}^{2-}$, $HCO_3{}^{-}$) inclusion in the crystal formation. The existence of carbonate ions in the initial Ca-rich aqueous solution for the Zn:CAp effectively leads to the carbonate HAp formation. Accordingly, the

nanoparticles have the lower content of phosphorous as compared with the typical HAp, assuming that the carbonate ions are replacing the phosphate ions in the structures. Thus, the Zn:CAp nanoparticles are thought to be B-type carbonate apatite [25], which is important for mimicking human bone mineral. The resultant (Zn + Ca)/P molar ratios for 0.0—Zn:HAp and 0.0—Zn:CAp were 1.64 and 1.94 and the molar ratio decreased with increasing the Zn ion amount. It was suggested that the carbonate ion inclusion with the Zn ion substitution induced the negative charge decrease caused by replacing phosphate ions to resultantly lose the positive charge (i.e., generating the Ca defects) for compensating. Therefore, the Zn substitution in the crystal was successfully achieved, and the weight percentage of Zn ions in the 10—Zn:HAp and 10—Zn:CAp nanoparticles contains 0.76 and 0.68 wt%, which are safe for cells in the animal body because of the toxic threshold at 1.5–2 wt%.

Figure 1 shows the FT-IR spectra of the Zn:HAp and Zn:CAp nanoparticles with the different Zn concentrations. The peak observed at around 3530 cm^{-1} is due to the presence of structural hydroxyl group in the HAp structure. The broadband at around 3400 cm^{-1} attributed to the surface OH groups on the nanoparticles as well as the adsorbed water molecules was observed, which was enhanced with increasing the Zn substitution. The bands at 1076 cm^{-1}, 1030 cm^{-1}, 957 cm^{-1}, 601 cm^{-1}, 572 cm^{-1}, and 460 cm^{-1} can be assigned to the P–O vibrations of the phosphate ions [1, 26, 27]. Although the phosphate bands of the Zn:CAp nanoparticles are almost the same as the Zn:HAp nanoparticles, the double bands at around 1440 and 1420 cm^{-1} are attributed to the carbonate ions (e.g., $HCO_3{}^{-}$, $CO_3{}^{2-}$) in the structures [25, 28] and strongly appeared in the Zn:CAp. The carbonate ions were derived from atmospheric carbon dioxide and dissolved into the solution. The bands at around 1440 and 1420 cm^{-1} are attributed to the symmetric mode of the C–O bond (ν_s) and the asymmetric mode of the same C–O bond (ν_{as}). The variation in the relative band intensity ratio (ν_s/ν_{as}) with increasing the initial Zn ion substitution is attributed to changes in the inclusion state of the carbonate ions in the HAp structure. The band at 957 cm^{-1} is assigned to a nondegenerated symmetric stretching mode of the P–O bond of the phosphate group, which was clearly observed in the Zn:CAp nanoparticles. The double bands at 601 cm^{-1} and 572 cm^{-1} are assigned to a triply degenerated bending mode

(a)

(b)

FIGURE 1: FT-IR spectra of the (a) Zn:HAp and (b) Zn:CAp nanoparticles with the different Zn concentrations.

(a)

(b)
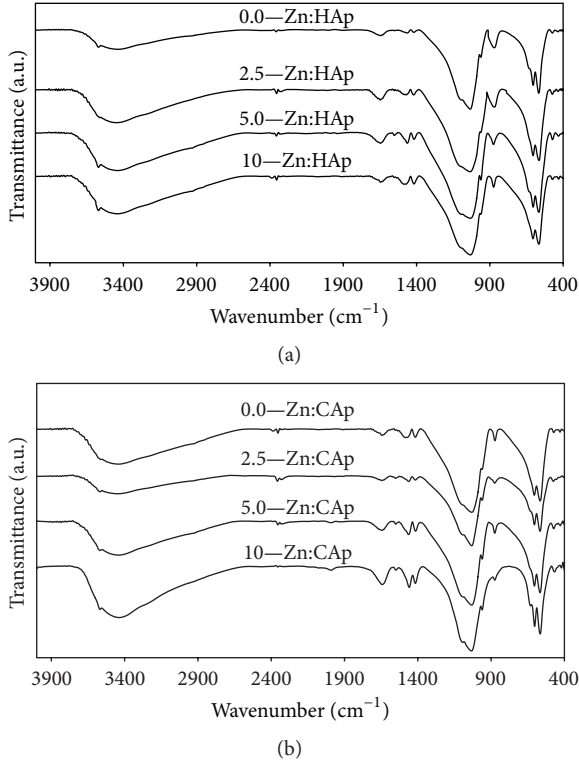
FIGURE 2: XRD patterns of the (a) Zn:HAp and (b) Zn:CAp nanoparticles with the different Zn concentrations.

TABLE 2: Lattice parameters and crystalline sizes of the Zn:HAp and Zn:CAp nanoparticles with the different Zn concentrations.

Sample	Lattice parameters		Crystalline sizes	
	a (Å)	c (Å)	d_{002} (nm)	d_{300} (nm)
0.0—Zn:HAp	9.40	6.88	40	20
2.5—Zn:HAp	9.42	6.88	24	5.7
5.0—Zn:HAp	9.33	6.84	14	5.4
10—Zn:HAp	9.28	6.83	13	5.0
0.0—Zn:CAp	9.43	6.91	34	15
2.5—Zn:CAp	9.29	6.91	21	6.0
5.0—Zn:CAp	9.27	6.84	20	5.6
10—Zn:CAp	9.24	6.70	18	4.6

of the O−P−O. The weak band at around 460 cm^{-1} is assigned to the components of the doubly degenerated bending mode in the phosphate ion.

3.2. Analysis of Crystalline Structures. Figure 2 shows the XRD patterns of the Zn:HAp and Zn:CAp nanoparticles with the different Zn concentrations. All the peaks were assigned to a HAp single phase (JCPDS number 09-0432). With the increase in the Zn ion substitution, the peaks are slightly broadening, which would be attributed to the decreased crystallinity by the Zn ion (radius: ca. 0.6 nm) substitution with Ca ion (radius: ca. 0.1 nm) in the HAp structure [29, 30].
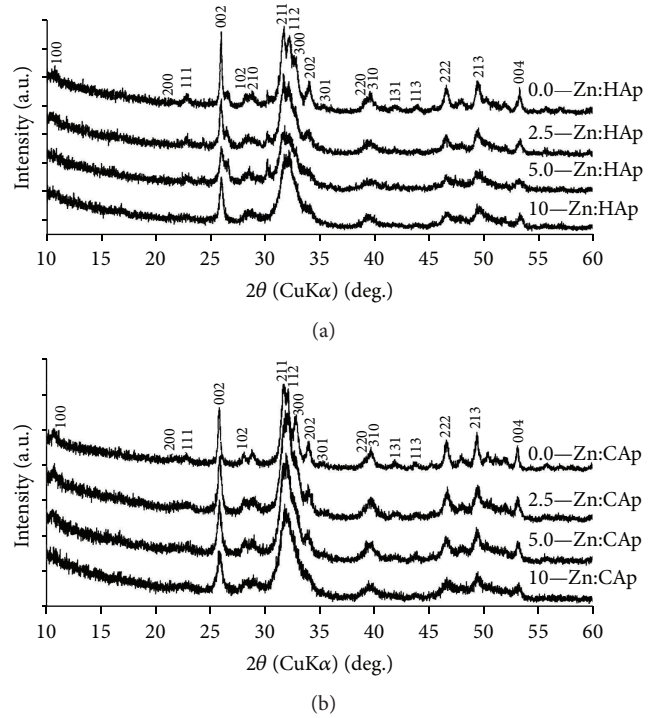
The calculated hexagonal unit cell (a and c) and crystalline sizes (d_{002} and d_{300}) are shown in Table 2. The 0.0—Zn:HAp and 0.0—Zn:CAp nanoparticles are a = 9.40 Å and c = 6.88 Å and a = 9.43 Å and c = 6.91 Å, respectively, which are almost similar to the literature of normal hydroxyapatite (a = 9.42 Å, c = 6.88 Å) [2]. The decrease in the a lattice parameter with increasing the Zn ion substation suggested that the replacement of Ca ions with Zn ion causes the defects as well as suppressing the crystal growth along with the a-plane [31]. Only in the Zn:CAp nanoparticles, c lattice parameter also decreased with increasing the Zn ion substitution, suggesting that the phosphate ions were replaced with carbonate ions in the c-plane surfaces to suppress the crystal growth along with the plane. Thus, the synthesis in the Zn:CAp can induce the higher replacement of the phosphate ions with carbonate ions to totally suppress both the a- and c-plane crystal growing, and the phenomena would make the crystalline size smaller in the Zn:CAp. The crystalline sizes (d_{300} and d_{002}) decreased with increasing the Zn ion substitution amount, indicating that the Zn ion addition suppresses the HAp crystal growth to form smaller crystals [29, 30, 32]. Thus, the Zn ion substitution suppressed the crystal growth by the exchange of the native Ca and phosphate ions at the near surfaces.

3.3. Investigation into Nanoscale Structures and Morphologies. The N$_2$ adsorption/desorption isotherms of the Zn:HAp and Zn:CAp nanoparticles are shown in Figure 3, and the S_{BET} and r_{BJH} values with the different Zn ion concentrations are summarized in Table 3. The S_{BET} value significantly increased
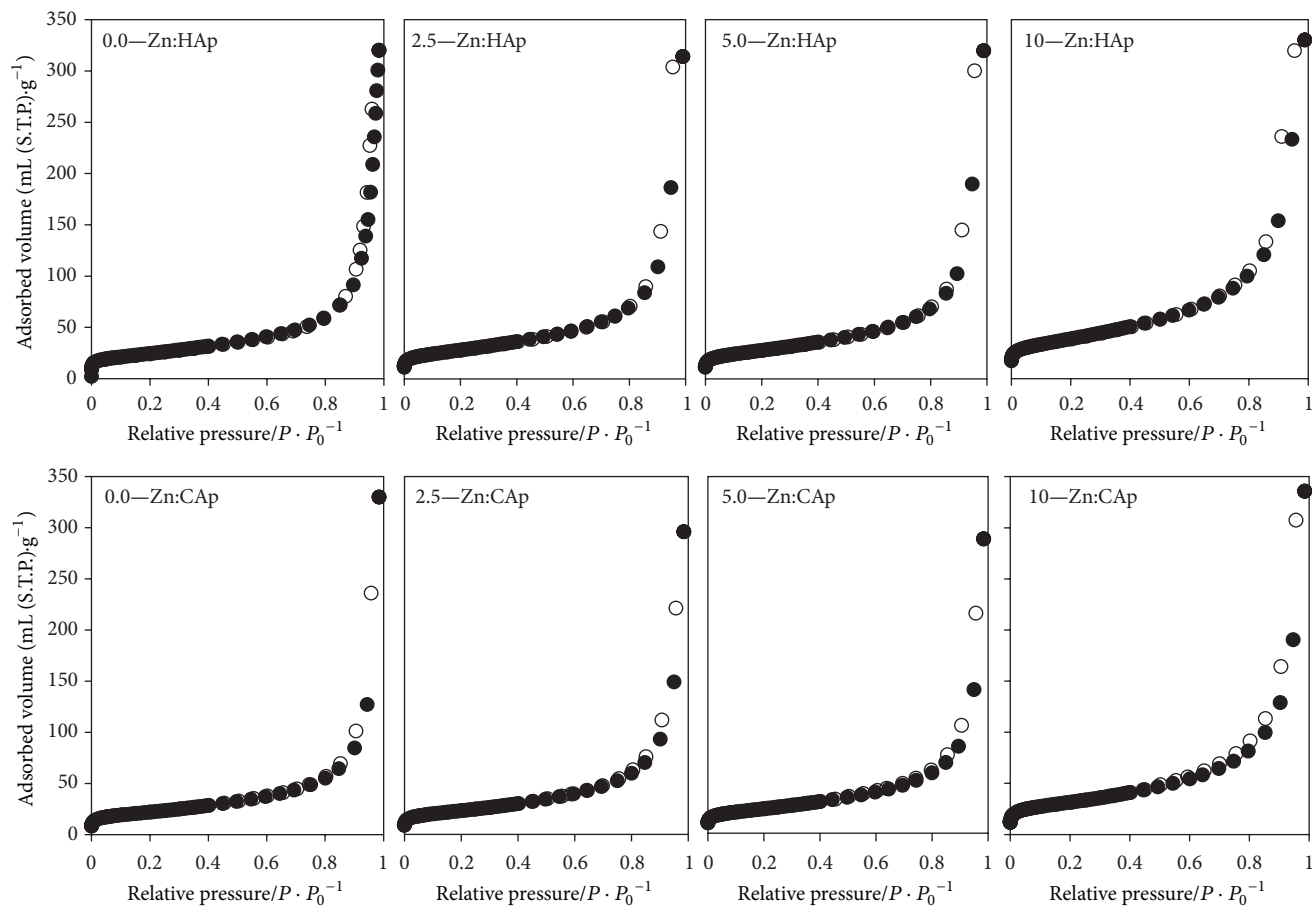
FIGURE 3: Nitrogen adsorption (closed circles) and desorption (open circles) isotherms of the Zn:HAp and Zn:CAp nanoparticles with the different Zn concentrations.

TABLE 3: S_{BET} and $2r_{BJH}$ values of the Zn:HAp and Zn:CAp nanoparticles with the different Zn concentrations.

Sample	S_{BET} (m$^2\cdot$g^{-1})	r_{BJH} (nm)
0.0—Zn:HAp	78.0	9.80
2.5—Zn:HAp	82.0	9.80
5.0—Zn:HAp	85.0	9.80
10—Zn:HAp	112	9.70
0.0—Zn:CAp	87.0	10.6
2.5—Zn:CAp	99.0	10.6
5.0—Zn:CAp	100	10.5
10—Zn:CAp	118	9.70

with increasing the Zn ion substitution, which would be attributed to the smaller nanocrystalline formation through the nucleation and crystal growth process accompanied with high surface concentration steps, kinks, and vacancies. All the samples give typical type III adsorption isotherms with a slight H3 hysteresis loop as defined by IUPAC [33], indicating the macropores and aggregation formed by the nanoparticles based on the adsorption on adsorbents with strong interactions as the unrestricted monolayer-multilayer adsorption state [34]. This result suggests the change in the

nanoparticle sizes as well as the aggregation states among the smaller-sized spherical nanoparticles. The hysteresis loop is gradually opening a little more with increasing the Zn ion substitution, indicating the aggregation states to form the mesoscale pores, suggesting the nanospaces confined by the nanoparticle aggregation form. The average pore sizes at 9-10 nm are almost the same with increasing the Zn ion substitution.

TEM images of the Zn:HAp and Zn:CAp nanoparticles with the different Zn ion concentrations are shown in Figure 4. All the nanoparticles exhibit the smaller crystalline sizes less than 100 nm. The crystal sizes observed in the TEM correspond to those calculated by the Scherrer equation, indicating the single crystal of one nanoparticle. In the 0.0— and 2.5—Zn:HAp nanoparticles significantly exhibit the needle-like shapes, and the needle-like shapes were changed to particulate shapes and aggregation states with increasing the Zn ion substitution. On the other hand, the Zn:CAp nanoparticles exhibit the particulate shapes at the lower Zn ion concentrations, and the higher concentration of Zn also induces the spherical shapes and aggregation states.

3.4. Cytotoxicity in Fibroblasts. Figure 5 shows the density and area of the adherent cells on the nanoparticle films.
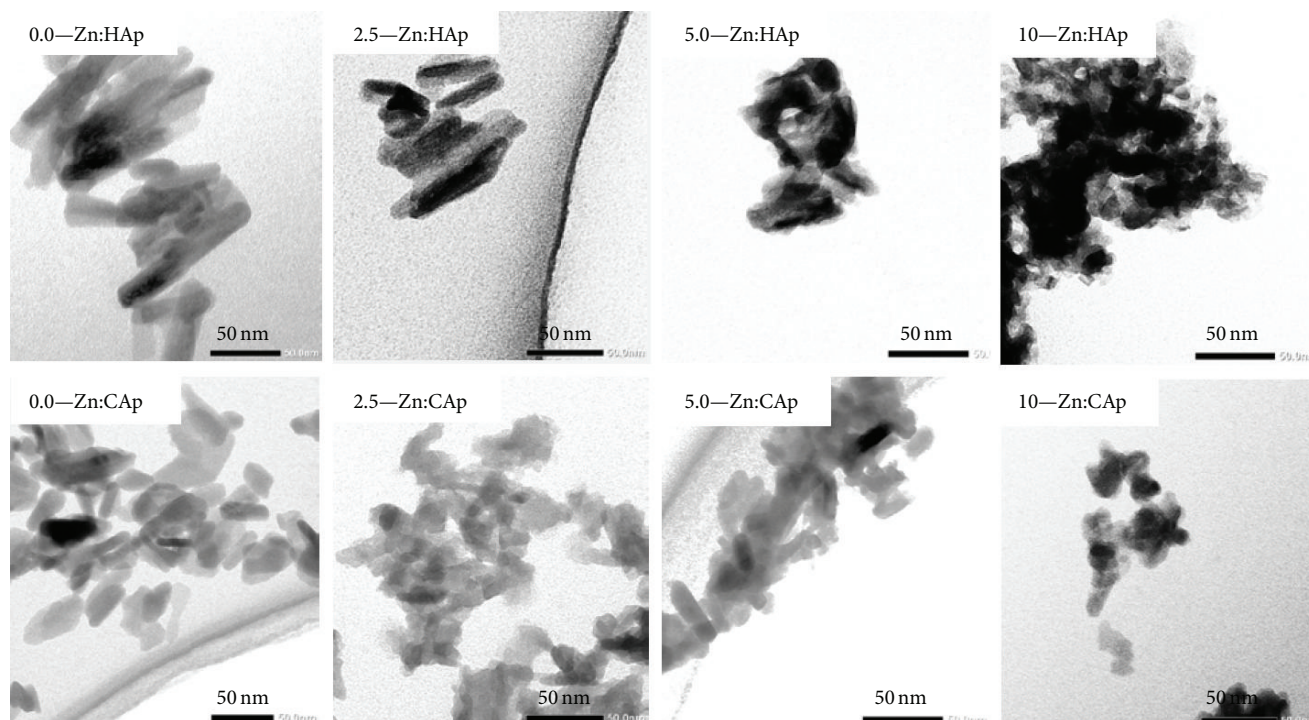
FIGURE 4: TEM images of the Zn:HAp and Zn:CAp nanoparticles with the different Zn concentrations.

The densities of cells on the Zn:CAp nanoparticle films are highest (Figure 5(a)), whereas the areas are almost the same among the nanoparticles (Figure 5(b)). In particular, the densities on the 5.0— and 10—Zn:CAp nanoparticle films are higher, indicating the good adhesion due to the carbonated and Zn-substituted surfaces. The cells on the Zn:HAp nanoparticles exhibited the spreading as shown in Figures 5(c)–5(j) which are the same as the cellular shapes on the reference silicone. In contrast, the cells on the 2.5—, 5.0—, and 10.0—Zn:CAp showed the uniaxial and fibrous spreading shapes. The cell survival is known to be affected by the adherent cell shapes and areas [14], indicating that the Zn:CAp nanoparticles would provide long cell survival without cytotoxicity. Therefore, the Zn:CAp nanoparticles could provide suitable surface properties for fibroblast interactions, suggesting both the carbonation and Zn substitution of HAp promote the fibroblast adhesion. Therefore, the optimized cytocompatible properties of the nanoparticles were successfully suggested, which can be useful as the implant surface modification. The electrophoretic fabrication of Zn:HAp and Zn:CAp nanoparticle films on silicone will be reported in the other journal soon by our laboratory to investigate the biological properties in detail.

4. Conclusions

The Zn-substituted HAp nanoparticles were successfully synthesized at the initial molar ratios of (Ca + Zn)/P at 1.67 and 2.00, providing the stoichiometric Zn:HAp and carbonate Zn:CAp nanoparticles, and the maximum Zn ion substitution in the structure is ca. 5 mol% by the XRF analysis.

The 10—Zn:HAp and 10—Zn:CAp nanoparticles contain 0.76 and 0.68 wt% of Zn at the maxima, respectively, which are safe for cells in the animal body. The increase in the Zn ion concentration significantly induced the inclusion of carbonate ions. The crystalline size decreased with the increasing Zn ion substitution, indicating the suppression of the crystal growth by the Zn ion addition to resultantly increase the specific surface area. TEM observation clearly indicated that the needle-like shape nanoparticles were changed to the particulate shapes with increasing the Zn ion substitution to form aggregation form with the mesostructures. Thus, the morphological control by the Zn substitution in stoichiometric and carbonate HAp nanoparticles was successfully achieved. Furthermore, all the nanoparticle films electrically plated on a silicone substrate give no cytotoxicity, and the Zn:CAp nanoparticle films significantly provided the bioactive properties for fibroblast ingrowth, suggesting the effect of Zn and carbonate ions on the cytocompatibility.

Conflict of Interests

The authors declare that there is no conflict of interests regarding the publication of this paper.
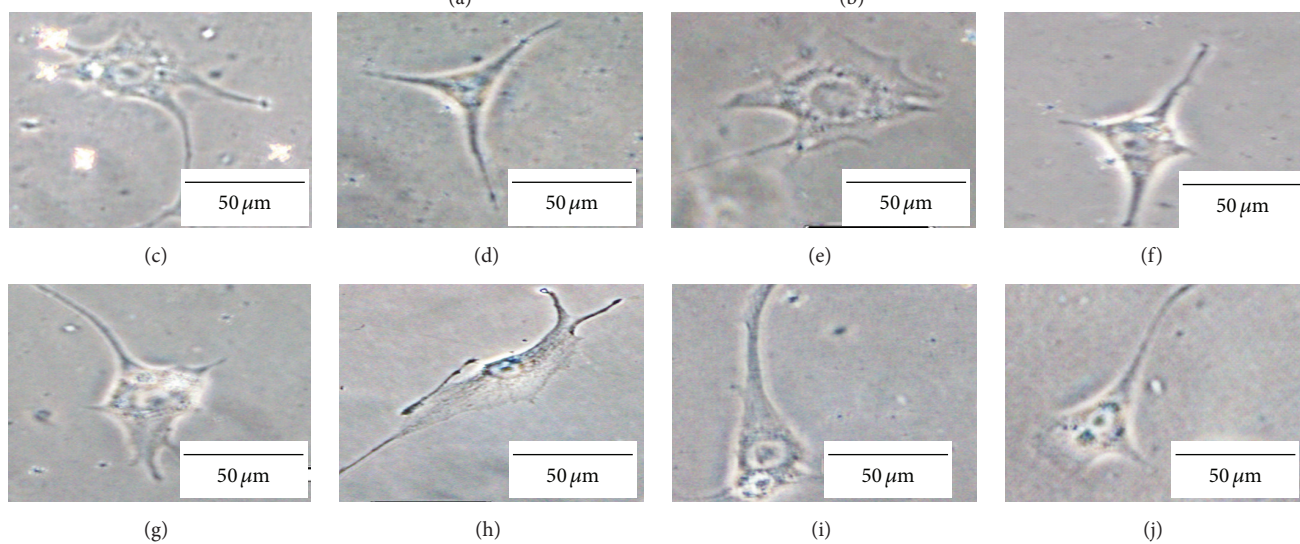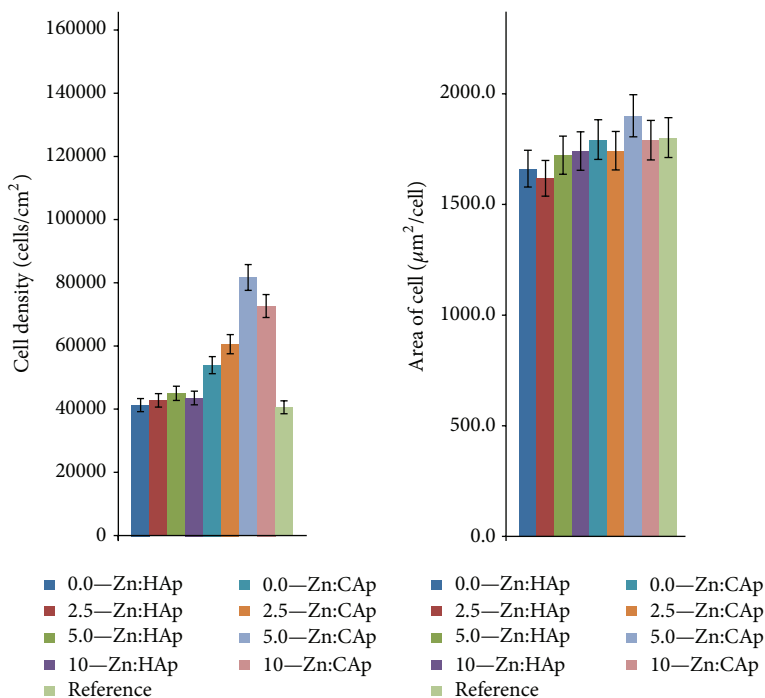
FIGURE 5: (a) Densities and (b) areas of the fibroblasts adhered on the Zn:HAp and Zn:CAp nanoparticle films with the different Zn concentrations and the reference silicone film and the optical microscope images of the fibroblasts adhered on (c, g) 0.0—, (d, h) 2.5—, (e, i) 5.0—, and (f, j) 10.0— (c–f) Zn:HAp and (g–j) Zn:CAp nanoparticle films at the culture time of 48 h.

References

[1] M. Tagaya, T. Ikoma, M. Takeguchi, N. Hanagata, and J. Tanaka, "Interfacial serum protein effect on biological apatite growth," *Journal of Physical Chemistry C*, vol. 115, no. 45, pp. 22523–22533, 2011.

[2] M. I. Kay, R. A. Young, and A. S. Posner, "Crystal structure of hydroxyapatite," *Nature*, vol. 204, no. 4963, pp. 1050–1052, 1964.

[3] M. Kikuchi, S. Itoh, S. Ichinose, K. Shinomiya, and J. Tanaka, "Self-organization mechanism in a bone-like hydroxyapatite/collagen nanocomposite synthesized in vitro and its biological reaction in vivo," *Biomaterials*, vol. 22, no. 13, pp. 1705–1711, 2001.

[4] A. Letic-Gavrilovic, A. Piattelli, and K. Abe, "Nerve growth factor β(NGF β) delivery via a collagen/hydroxyapatite (Col/HAp) composite and its effects on new bone ingrowth," *Journal of Materials Science: Materials in Medicine*, vol. 14, no. 2, pp. 95–102, 2003.

[5] S. S. Liao and F.-Z. Cui, "In vitro and in vivo degradation of mineralized collagen-based composite scaffold: nanohydroxyapatite/collagen/poly(L-lactide)," *Tissue Engineering*, vol. 10, no. 1-2, pp. 73–80, 2004.

[6] S. Yunoki, T. Ikoma, A. Monkawa et al., "Control of pore structure and mechanical property in hydroxyapatite/collagen

composite using unidirectional ice growth," *Materials Letters*, vol. 60, no. 8, pp. 999–1002, 2006.

[7] W. Paul and C. P. Sharma, "Ceramic drug delivery: a perspective," *Journal of Biomaterials Applications*, vol. 17, no. 4, pp. 253–264, 2003.

[8] H.-W. Kim, J. C. Knowles, and H.-E. Kim, "Porous scaffolds of gelatin–hydroxyapatite nanocomposites obtained by biomimetic approach: characterization and antibiotic drug release," *Journal of Biomedical Materials Research B: Applied Biomaterials*, vol. 74, no. 2, pp. 686–698, 2005.

[9] Y. Mizushima, T. Ikoma, J. Tanaka et al., "Injectable porous hydroxyapatite microparticles as a new carrier for protein and lipophilic drugs," *Journal of Controlled Release*, vol. 110, no. 2, pp. 260–265, 2006.

[10] T. Ikomal, T. Tonegawa, H. Watanaba, G. Chen, J. Tanaka, and Y. Mizushima, "Drug-supported microparticles of calcium carbonate nanocrystals and its covering with hydroxyapatite," *Journal of Nanoscience and Nanotechnology*, vol. 7, no. 3, pp. 822–827, 2007.

[11] M. Tagaya, S. Motozuka, T. Kobayashi, T. Ikoma, and J. Tanaka, "Mechanochemical preparation of 8-hydroxyquinoline/hydroxyapatite hybrid nanocrystals and their photofunctional interfaces," *Industrial and Engineering Chemistry Research*, vol. 51, no. 34, pp. 11294–11300, 2012.

[12] C. Yongli, Z. Xiufang, G. Yandao, Z. Nanming, Z. Tingying, and S. Xinqi, "Conformational changes of fibrinogen adsorption onto hydroxyapatite and titanium oxide nanoparticles," *Journal of Colloid and Interface Science*, vol. 214, no. 1, pp. 38–45, 1999.

[13] M. Tagaya, T. Ikoma, T. Takemura et al., "Detection of interfacial phenomena with osteoblast-like cell adhesion on hydroxyapatite and oxidized polystyrene by the quartz crystal microbalance with dissipation," *Langmuir*, vol. 27, no. 12, pp. 7635–7644, 2011.

[14] C. S. Chen, M. Mrksich, S. Huang, G. M. Whitesides, and D. E. Ingber, "Geometric control of cell life and death," *Science*, vol. 276, no. 5317, pp. 1425–1428, 1997.

[15] F. Bir, H. Khireddine, A. Touati, D. Sidane, S. Yala, and H. Oudadesse, "Electrochemical depositions of fluorohydroxyapatite doped by Cu^{2+}, Zn^{2+}, Ag^+ on stainless steel substrates," *Applied Surface Science*, vol. 258, no. 18, pp. 7021–7030, 2012.

[16] E. Boanini, M. Gazzano, and A. Bigi, "Ionic substitutions in calcium phosphates synthesized at low temperature," *Acta Biomaterialia*, vol. 6, no. 6, pp. 1882–1894, 2010.

[17] G. S. Kumar, A. Thamizhavel, Y. Yokogawa, S. N. Kalkura, and E. K. Girija, "Role of material processing on the thermal stability and sinterability of nanocrystalline hydroxyapatite," *Materials Chemistry and Physics*, vol. 134, no. 2, pp. 1127–1135, 2012.

[18] L. C. Ann, S. Mahmud, and S. K. M. Bakhori, "Electron spectroscopy imaging and surface defect configuration of zinc oxide nanostructures under different annealing ambient," *Applied Surface Science*, vol. 265, pp. 137–144, 2013.

[19] E. S. Thian, T. Konishi, Y. Kawanobe et al., "Zinc-substituted hydroxyapatite: a biomaterial with enhanced bioactivity and antibacterial properties," *Journal of Materials Science: Materials in Medicine*, vol. 24, no. 2, pp. 437–445, 2013.

[20] Y.-T. Huang, M. Imura, Y. Nemoto, C.-H. Cheng, and Y. Yamauchi, "Block-copolymer-assisted synthesis of hydroxyapatite nanoparticles with high surface area and uniform size," *Science and Technology of Advanced Materials*, vol. 12, no. 4, Article ID 045005, 2011.

[21] A. Monshi, M. R. Foroughi, and M. R. Monshi, "Modified scherrer equation to estimate more accurately nano-crystallite size using XRD," *World Journal of Nano Science and Engineering*, vol. 2, no. 3, pp. 154–160, 2012.

[22] N. Puvvada, P. K. Panigrahi, and A. Pathak, "Room temperature synthesis of highly hemocompatible hydroxyapatite, study of their physical properties and spectroscopic correlation of particle size," *Nanoscale*, vol. 2, no. 12, pp. 2631–2638, 2010.

[23] S. Brunauer, P. H. Emmett, and E. Teller, "Adsorption of gases in multimolecular layers," *Journal of the American Chemical Society*, vol. 60, no. 2, pp. 309–319, 1938.

[24] E. P. Barrett, L. G. Joyner, and P. P. Halenda, "The determination of pore volume and area distributions in porous substances. I. Computations from nitrogen isotherms," *Journal of the American Chemical Society*, vol. 73, no. 1, pp. 373–380, 1951.

[25] J. Barralet, S. Best, and W. Bonfield, "Carbonate substitution in precipitated hydroxyapatite: an investigation into the effects of reaction temperature and bicarbonate ion concentration," *Journal of Biomedical Materials Research*, vol. 41, no. 1, pp. 79–86, 1998.

[26] S. Koutsopoulos, "Synthesis and characterization of hydroxyapatite crystals: a review study on the analytical methods," *Journal of Biomedical Materials Research*, vol. 662, no. 4, pp. 600–612, 2012.

[27] R. K. Brundavanam, G. E. J. Poinern, and D. Fawcett, "Modelling the crystal structure of a 30 nm sized particle based hydroxyapatite powder synthesized under the influence of ultrasound irradiation from X-ray powder diffraction data," *American Journal of Materials Science*, vol. 3, no. 4, pp. 84–90, 2013.

[28] M. Markovic, B. O. Fowler, and M. S. Tung, "Preparation and comprehensive characterization of a calcium hydroxyapatite reference material," *Journal of Research of the National Institute of Standards and Technology*, vol. 109, no. 6, pp. 553–568, 2004.

[29] Y. J. Lee, E. J. Elzinga, and R. J. Reeder, "Sorption mechanisms of zinc on hydroxyapatite: systematic uptake studies and EXAFS spectroscopy analysis," *Environmental Science & Technology*, vol. 39, no. 11, pp. 4042–4048, 2005.

[30] Y. Fenga, J.-L. Gonga, G.-M. Zenga et al., "Adsorption of Cd (II) and Zn (II) from aqueous solutions using magnetic hydroxyapatite nanoparticles as adsorbents," *Chemical Engineering Journal*, vol. 162, no. 2, pp. 487–494, 2010.

[31] T. Ikoma, A. Yamazaki, S. Nakamura, and M. Akao, "Preparation and structure refinement of monoclinic hydroxyapatite," *Journal of Solid State Chemistry*, vol. 144, no. 2, pp. 272–276, 1999.

[32] T. Furuzono, P.-L. Wang, A. Korematsu et al., "Physical and biological evaluations of sintered hydroxyapatite/silicone composite with covalent bonding for a percutaneous implant material," *Journal of Biomedical Materials Research—Part B: Applied Biomaterials*, vol. 65, no. 2, pp. 217–226, 2003.

[33] K. S. W. Sing, D. H. Everett, R. A. W. Haul et al., "Reporting physisorption data for gas/solid systems with special reference to the determination of surface area and porosity," *Pure and Applied Chemistry*, vol. 57, no. 4, pp. 603–619, 1985.

[34] M. Tagaya, T. Ikoma, S. Migita et al., "Fetal bovine serum adsorption onto hydroxyapatite sensor monitoring by quartz crystal microbalance with dissipation technique," *Materials Science and Engineering B: Solid-State Materials for Advanced Technology*, vol. 173, no. 1–3, pp. 176–181, 2010.